On the Initiation of an Isolated Heavy-Rain-Producing Storm near the Central Urban Area of Beijing Metropolitan Region

HUIQI LI

Key Laboratory of Cloud-Precipitation Physics and Severe Storms (LACS), Institute of Atmospheric Physics, Chinese Academy of Sciences, and University of Chinese Academy of Sciences, Beijing, China

XIAOPENG CUI

Key Laboratory of Cloud-Precipitation Physics and Severe Storms (LACS), Institute of Atmospheric Physics, Chinese Academy of Sciences, and University of Chinese Academy of Sciences, Beijing, and Collaborative Innovation Center on Forecast and Evaluation of Meteorological Disasters, Nanjing University of Information Science and Technology, Nanjing, China

DA-LIN ZHANG

State Key Laboratory of Severe Weather, Chinese Academy of Meteorological Sciences, Beijing, China, and Department of Atmospheric and Oceanic Science, University of Maryland, College Park, College Park, Maryland

(Manuscript received 29 March 2016, in final form 22 September 2016)

ABSTRACT

An isolated heavy-rain-producing thunderstorm was unexpectedly initiated in the afternoon of 9 August 2011 near the central urban area of the Beijing metropolitan region (BMR), which occurred at some distance from BMR's northwestern mountains and two preexisting mesoscale convective systems (MCSs) to the west and north, respectively. An observational analysis shows the presence of unfavorable quasigeostrophic conditions but a favorable regional environment for the convective initiation (CI) of thunderstorms. A nested-grid cloud-resolving model simulation of the case with the finest 1.333-km resolution is performed to examine the CI of the thunderstorm and its subsequent growth. Results reveal that the growth of the mixed boundary layer, enhanced by the urban heat island (UHI) effects, accounts for the formation of a thin layer of clouds at the boundary layer top at the CI site and nearby locations as well as on the upslope sides of the mountains. It takes about 36 min for the latent-heating-driven updraft to penetrate through a 1-km "lid" layer above before the formation of the thunderstorm. However, this storm may not take place without sustained low-level convergence of a prevailing southerly flow with a northerly flow ahead of a cold outflow boundary associated with the northern MCS. The latter is driven by the latent heating of the shallow layer of clouds during the earlier CI stage and then a cold mesohigh underneath the northern MCS. This study indicates the important roles of the urban effects, mountain morphology, and convectively generated pressure perturbations in determining the CI location and timing of isolated thunderstorms during the summer months.

1. Introduction

Although considerable progress has been made in predicting and understanding the development of mesoscale convective systems (MCSs), our ability to predict the timing and location of new convection, hereafter referred to as convective initiation (CI), is very limited. This is especially true for the CI of isolated convective storms. Previous studies have shown clearly the CI of MCSs along the convergence zones in the planetary boundary layer (PBL), frontal zones, and drylines (e.g., Byers and Rodebush 1948; Rhea 1966; Hane et al. 1993; Purdom 1976; Wilson and Schreiber 1986; Koch and Ray 1997; Wilson and Megenhardt 1997; Ziegler and Rasmussen 1998). However, predicting the precise location of CI remains to be a challenging task. This is because the

Corresponding author address: Dr. Xiaopeng Cui, Key Laboratory of Cloud-Precipitation Physics and Severe Storms (LACS), Institute of Atmospheric Physics, Chinese Academy of Sciences, Beijing 100029, China.
E-mail: xpcui@mail.iap.ac.cn

DOI: 10.1175/MWR-D-16-0115.1

© 2017 American Meteorological Society

location of CI is influenced by spatial variability of temperature and moisture in the PBL (e.g., Mueller et al. 1993; Weckwerth et al. 1996), variable terrain, or inhomogeneous surface characteristics (e.g., Clark and Arritt 1995; Weckwerth 2000; Baker et al. 2001; Lin et al. 2001) that are often on scales too small to be resolved by conventional observations and numerical weather prediction (NWP) models. Thus, several field campaigns, such as the Convection Initiation and Downburst Experiment (CINDE; Wilson et al. 1988), the International H_2O Project (IHOP_2002; Weckwerth et al. 2004), the Convective Storm Initiation Project (Browning et al. 2007), and the Convective and Orographically Induced Precipitation Study (COPS; Wulfmeyer et al. 2008), have been conducted in the past decades to obtain high-resolution observations for CI investigations. A series of the observational studies from these field campaigns reveals that some finescale features (e.g., convergence lines, horizontal rolls, misocyclones, and enhanced moisture supply) play an important role in determining the precise location and timing of CI. That is, the intersection of convergence lines and horizontal rolls with enhanced updrafts encourages CI (Wilson et al. 1992), enhanced water vapor provides a favorable condition for CI (Behrendt et al. 2011; Van Baelen et al. 2011), and misocyclones tend to distort drylines and the related moisture distribution, producing favorable regions for CI where moisture pockets align with the surface rotational instabilities along the convergence lines (Murphey et al. 2006).

On the other hand, NWP models have been widely used to study CI, although predicting its right location/timing by today's operational NWP models still remains a great challenge. The CI problem used to be examined as a convective trigger function parameterized in terms of grid-scale vertical motion and moisture convergence in coarse-resolution NWP models (e.g., Zhang and Fritsch 1986; Kain and Fritsch 1992). In recent years, cloud-resolving NWP models have made it possible to study more realistically different processes leading to the CI of isolated thunderstorms or MCSs. Lean et al. (2009) performed a series of numerical experiments with the Met Office Unified Model (MetUM) to examine the effect of roughness, diurnal heating, and orography on the CI of an isolated thunderstorm in southern England. Wang and Xue (2012) performed a CI-modeling study of an MCS occurring during IHOP_2002, and found that enhanced vertical motion and upward moisture advection at the intercepting point with a dryline provide the most favorable conditions for CI. Weckwerth et al. (2014) simulated an orographically induced CI event during COPS, and noted that convergence along the sloping Vosges Mountains leads to the CI and that the spatial variability of buoyancy and lids influences the location and timing of the CI.

Previous observational and modeling studies have also revealed that the CI and subsequent development of deep convection could be influenced by preexisting MCSs. For instance, CI may take place along cold outflow boundaries resulting from existing precipitation systems (Wilhelmson and Chen 1982; Wilson and Schreiber 1986; Weckwerth and Wakimoto 1992; Wilson and Mueller 1993). Khairoutdinov and Randall (2006) designed sensitivity experiments to explain the key effect of cold pools on the CI of shallow to deep convection. Lima and Wilson (2008) showed that convective storms could be easily triggered by gust fronts or colliding outflow boundaries.

The CI and subsequent generation of local heavy rainfall events over the Beijing metropolitan region (BMR) have attracted considerable attention in recent years as they have often resulted in severe urban inundation and landslides in mountainous regions, exerting a great threat to the capital of China. Because of the complex topography of Mt. Yan to the north and Mt. Taihang to the west as well as diverse underlying surfaces, the distribution of CI locations over the BMR is highly variable and difficult to predict by today's operational NWP models and experienced forecasters. Wang and Sun (2008) found the occurrence of CI in coincidence with topographically induced convergence over the BMR's western mountains, with its subsequent convective developments supported by the enhanced warming of the urban PBL. Wilson et al. (2010) studied the development of convective storms over the BMR, and found that various boundary layer convergence lines of different origins such as gust fronts, sea breezes, and colliding boundaries play an important role in the initiation and evolution of the storms. Wang et al. (2011) and Zhang et al. (2013) showed that the low-level warm and moist easterly flow is a key factor in determining the CI and organization of MCSs over the BMR. Zhang et al. (2011) used idealized numerical simulations to illustrate the possible roles of moisture content in the PBL in the formation of dry convection and the CI of thunderstorms. An observational study of Zhang et al. (2014) suggested that cold outflows from existing MCSs and topographical forcing are the two deterministic factors influencing the locations of CI over the BMR. Xiao et al. (2015) described the crucial roles of cold pools in accounting for the development of convective storms on the downslope side of the BMR's western mountains. Nevertheless, few studies have been performed to examine the CI processes leading to the generation of isolated storms over the BMR, especially those that are far away from significant topographical influences.

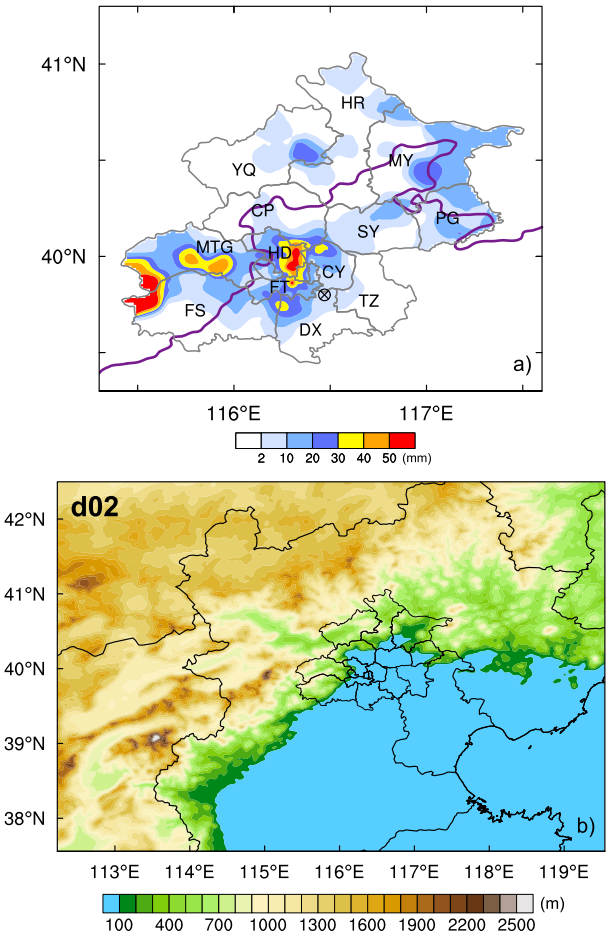

FIG. 1. (a) Distribution of the 3-h accumulated precipitation (color shaded, mm) from 1600 to 1900 LST 9 Aug 2011. BMR's district names are abbreviated in alphabetical order as follows: Changping (CP), Chaoyang (CY), Daxing (DX), Fangshan (FS), Fengtai (FT), Haidian (HD), Huairou (HR), Mentougo (MTG), Miyun (MY), Pinggu (PG), Shunyi (SY), Tongzhou (TZ), and Yanqing (YQ); the BMR's two small eastern and western (central business) districts, located to HD's immediate southeast and Shijingshan District to HD's immediate southwest are not denoted. The Beijing radar station and upper-air observations are collocated, as denoted by a crossed circle in northern Daxing. A thick purple line denotes the 200-m terrain elevation; similarly for the rest of the figures. (b) A one-way nested, 1.333-km resolution inner model domain with terrain elevations plotted (shadings, m). The outer 4-km resolution domain covers an area of 3160 km × 2548 km, with the lower-left corner at 27.4°N, 100.1°E and the upper-right corner at 49.6°N, 137.6°E (not shown).

Thus, the purpose of this study is to investigate the CI of a local heavy rain event associated with an isolated convective storm near the central urban area of the BMR on 9 August 2011 (Fig. 1a), hereafter referred to as the 9 August heavy rainfall event. The reasons for choosing this case are as follows. First, the storm of interest was unexpectedly initiated in isolation near the BMR's central urban area, which was far away from the BMR's northwestern mountains and the direct influences of two preexisting MCSs. Second, it grew rapidly after its formation, unlike the other scattered cloud systems in the urban PBL, and generated heavy rainfall after merging with an approaching MCS, seriously hindering the BMR's traffic during rush hours. Through the analyses of all available observations and numerical model simulations, we wish to answer the following questions: Why was the storm initiated in isolation and how did the CI occur? What are the pertinent environmental and local conditions accounting for the storm's CI and subsequent growth? What determines the CI location and timing of the storm?

The next section provides an observational analysis of the 9 August heavy rainfall event using the European Centre for Medium-Range Weather Forecasts (ECMWF) interim reanalysis (ERA-Interim), upper-air soundings, radar reflectivity, and dense surface observations over the BMR. Section 3 describes the model configuration and verifications. Section 4 shows the CI processes leading to the formation of clouds and subsequent convective outbreak of the storm, based on the model simulations. A summary and conclusions are given in the final section.

2. Observational analysis

The 9 August heavy rainfall event hit the BMR's central urban area in the late afternoon, mainly during the period of 1600–1900 LST (local standard time = UTC + 8 h), causing serious traffic jams during rush hours. Eight automatic weather stations (AWSs) in the Haidian (HD) District recorded an hourly rainfall amount of over 20 mm from 1700 to 1800 LST, and two of them recorded hourly rainfall amounts exceeding 50 mm (Fig. 1a). Frequent lightning activity was also observed during this period. Such a local heavy rain event is common in the BMR during summer months in recent years, which has imposed serious challenges to local weather forecasters in nowcasting the occurrence of such events.

a. Synoptic background

The large-scale environment at 1400 LST 9 August 2011 was characterized with a deep 500-hPa trough extending from the northeastern China to the Korean and Shandong peninsulas, and a high pressure center at the border of Mongolia and northern China. The BMR was situated in the cold sector with a cold center at about 500 km to the west, and it was influenced by weak northwesterly flows behind the trough axis (Fig. 2a). At 850 hPa (Fig. 2b), the elevated topography to the west

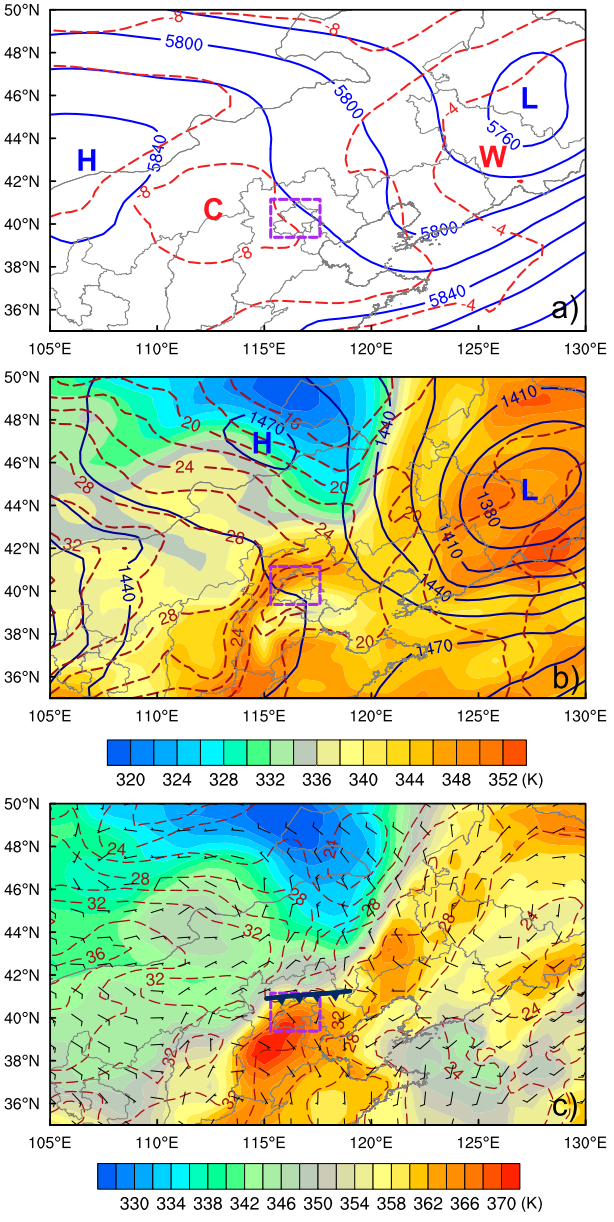

FIG. 2. The ECMWF's ERA-Interim at 1400 LST 9 Aug 2011. (a) Geopotential height (solid blue lines at intervals of 20 gpm) and temperature (dashed red lines at intervals of 2°C) at 500 hPa. (b) Geopotential height (solid blue lines at intervals of 15 gpm), temperature (dashed red lines at intervals of 2°C), and equivalent potential temperature (θ_e in K, shaded) at 850 hPa. (c) The 2-m temperature (dashed red lines at intervals of 2°C), θ_e (shaded, K), and 10-m winds (a full barb is 5 m s^{-1}). The dashed purple rectangle denotes the position of the BMR. Letters, "H," "L," "W," and "C" denote the centers of a high and low pressure system, and warm and cold air, respectively. Note the distribution of a surface cold front along the northern edge of the BMR.

generated large temperature gradients with a narrow tongue of high-θ_e (equivalent potential temperature) air along the southwest–northeast-oriented mountain slopes. Meanwhile, significant northeasterly cold and

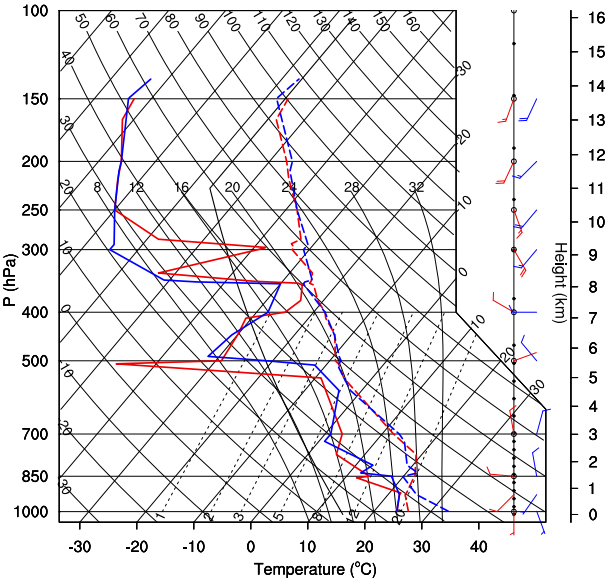

FIG. 3. Soundings taken at the BMR's southern observatory (see Fig. 1a for its location) at 0800 (red) and 1400 LST (blue) 9 Aug 2011.

lower-θ_e air advection occurred to the east of a high pressure system that was centered in eastern Mongolia. This cold and lower-θ_e air advection could be also clearly seen in the surface northerly flows, extending from eastern Mongolia to the BMR's northern region (Fig. 2c). Of relevance to the CI in the present case was the presence of a high-θ_e tongue associated with south to southeasterly flows occurring to the BMR's south over the plains. These two different air masses met just near the BMR's northern boundary, forming a thermal boundary, as indicated by a frontal symbol in Fig. 2c, which could clearly facilitate the initiation and subsequent organization of deep convection.

An early morning sounding taken at the BMR's southern observatory (Fig. 3), which was located in the low-level southerly warm sector, showed a stable layer from 925 hPa up to about 850 hPa and a deep dry layer aloft. An inversion with the bottom at 850 hPa was seen at 1400 LST due to the daytime development of a mixed layer. As the PBL grew, the lapse rate below $z = 1$ km became slightly superadiabatic, while little changes occurred above 700 hPa between 0800 and 1400 LST. As a result, the convective available potential energy (CAPE) increased from 1630 J kg^{-1} at 0800 LST to 2826 J kg^{-1} at 1400 LST, but still with some convective inhibition (CIN). Figure 3 also shows the veering of a southeasterly wind at the surface to a north-northwesterly wind at 850 hPa, and a north-northeasterly wind at 700 hPa and then slow backing aloft (e.g., at 1400 LST), indicating again the presence of weak warm advection in the lower

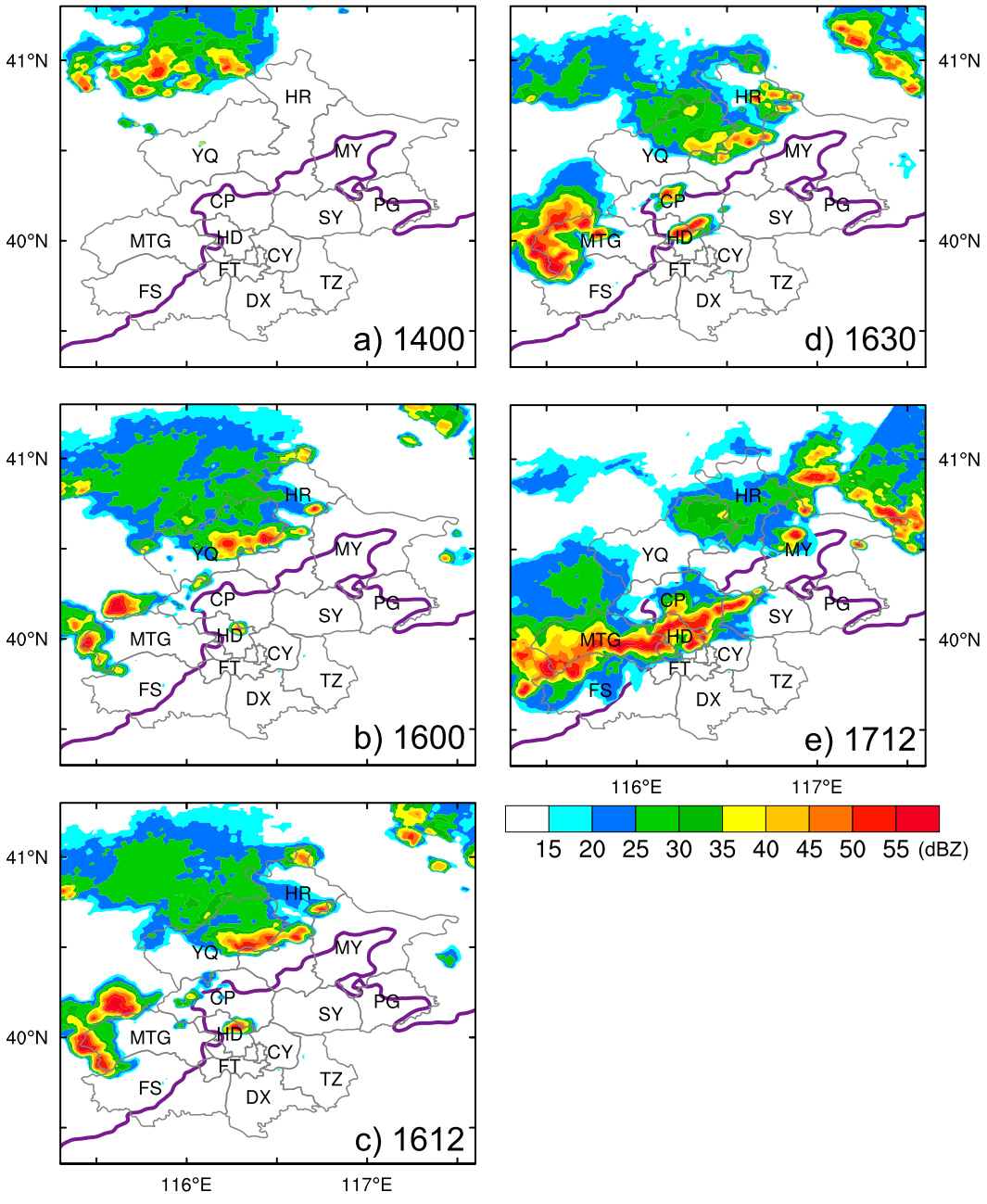

FIG. 4. Radar reflectivity composite (dBZ) observed by Beijing's radar site (see Fig. 1a for its location) at (a) 1400, (b) 1600, (c) 1612, (d) 1630, and (e) 1712 LST 9 Aug 2011.

troposphere (as also indicated in Fig. 2c) and cold advection above, notwithstanding relatively weak.

b. Radar reflectivity

Radar reflectivity at 1400 LST (Fig. 4a) showed the development of an MCS on the BMR's northwest, hereafter referred to as the northern MCS, which coincided with the distribution of the above-mentioned thermal boundary. Few radar echoes could be seen over the BMR at this time. However, an isolated convective storm with the maximum reflectivity exceeding 45 dBZ began to emerge at the HD–Changping (CP) border by 1600 LST (Fig. 4b), as the northern MCS moved into the BMR from its northwest. Meanwhile, several thunderstorms were also initiated over the BMR's western mountainous boundary. Although the isolated storm at the HD–CP border was much smaller in coverage than the western storms, it resulted in heavy rainfall over the

southern HD District (Figs. 4c–e and Fig. 1a). Thus, its initiation is our major concern from now on.

The western storms appeared to account for heavy rainfall in Mentougo (MTG) and Fangshan (FS) after their merging with the HD storm around 1712 LST (Fig. 4e). The isolated HD storm expanded both northeastward and southwestward (Figs. 4c,d). Despite its small coverage, the AWSs captured its associated rainfall starting from 1600 LST. The isolated storm finally merged with the western storms to form a well-organized convective line at 1712 LST (Fig. 4e), dropping more than 20 mm rainfall in less than an hour. In contrast, the northern MCS moved eastward across the BMR's northern districts and weakened subsequently after dropping 20–30-mm rainfall in Yanqing (YQ) and Huairou (HR). Given their distances of about 50 km away from HD, respectively, one may ask the following question: Would the northern MCS and western storms have any impact on the CI and subsequent growth of the HD storm? This question will also be addressed in the next section as one of the objectives of this study.

c. *Surface observations*

A surface analysis at 1400 LST, given in Fig. 5a, shows dominant southerly (10 m) surface winds (V_{SFC}) in the BMR's plain areas (also see Fig. 3), and up-valley flows in various directions in the mountainous regions, depending on the local mountain valley orientations (Whiteman 2000). The up-valley flows and the various surface properties appeared to account for the shift of the southerly flow to an easterly flow toward the "northwestward-concaved valley" over the HD and CP Districts at 1400 LST. The surface layer θ_e over the BMR's plain area was on average greater than 366 K, based on the 2-m AWS temperature of warmer than 30°C and specific humidity of more than 18 g kg^{-1}. Of interest is the development of several centers greater than θ_e = 374 K, three of which were persistently located around the HD–CP–Chaoyang (CY) border, and along the upslope sides of the northern and northeastern mountains, respectively (Figs. 5a–e). Over the HD District, the surface temperature and specific humidity reached over 34°C and 22 g kg^{-1}, respectively, prior to the CI (not shown). Although localized convergence was scattered over the BMR, more favorable surface convergence, as indicated by intersecting streamlines, coincided with the above-mentioned high-θ_e center around the HD–CP–CY border, which is located in the "wake" of the BMR's central business districts. Given the well-developed mixed layer and conditional instability (Fig. 3), the surface flow conditions appeared to favor the development of scattered storms, with an isolated storm coinciding with the local converging high-θ_e center around the HD–CP–CY border.

Figure 5b provides the first evidence of the northern MCS entering the BMR, as shown by divergent outflows of lower than θ_e = 340-K air, corresponding to colder than 24°C and drier than 12 g kg^{-1} air (not shown), in the northwestern YQ District where a narrow outflow boundary is clearly delineated. The low-θ_e outflows expanded rapidly into the BMR's northwestern districts. Of interest was the gradual retreat of south-to-southeasterly winds to the plain regions, except for MTG and FS Districts where the storms were still over the mountainous regions to the west of MTG District and hardly affected the up-valley winds (Figs. 5c–e). Instead, downslope flows occurred much ahead of the low-θ_e outflows associated with the northern MCS. As a result, by 1540 LST, a surface confluence zone of the two different flows took place at the foothills of lower than 200-m altitude, with an enhanced convergence center in HD District prior to the CI occurrence (Figs. 5c–e).

The above analyses reveal that the large-scale quasi-geostrophic conditions were unfavorable for organized convective development, but the regional-scale lower-tropospheric environment appeared to be favorable for CI, at least the presence of conditional instability and higher than θ_e = 374-K air as well as sustained surface convergence. The resulting convective event was characterized by an isolated convective storm that produced the 9 August heavy rainfall event during 2–3 late-afternoon hours. However, the above analyses could not reveal what processes generated the downslope flows, leading to the presence of the sustained convergence with the south-to-southeasterly flows and the subsequent CI in the HD District. Furthermore, what local processes or conditions, such as the low-level forcing, moisture content, CAPE, could facilitate the generation of heavy rainfall in the HD District? To address the above question and the questions raised earlier, we have to invoke high-resolution cloud-resolving simulations of the case.

3. Model configuration and verification

In this section, we describe the model configuration for the case simulation, and then validate the simulated convective events against radar observations, and high-resolution AWS data as much as possible before the model output could be used to study the isolated CI and rainfall production associated with the 9 August heavy rainfall event.

a. *Model configuration*

In this study, the processes leading to the 9 August heavy rainfall event are examined using one-way, two nested grids (4/1.333 km) of version 3.5.1 of the Weather Research and Forecasting (WRF) Model (Skamarock et al. 2008) with 50 vertical levels. The outer 4-km and

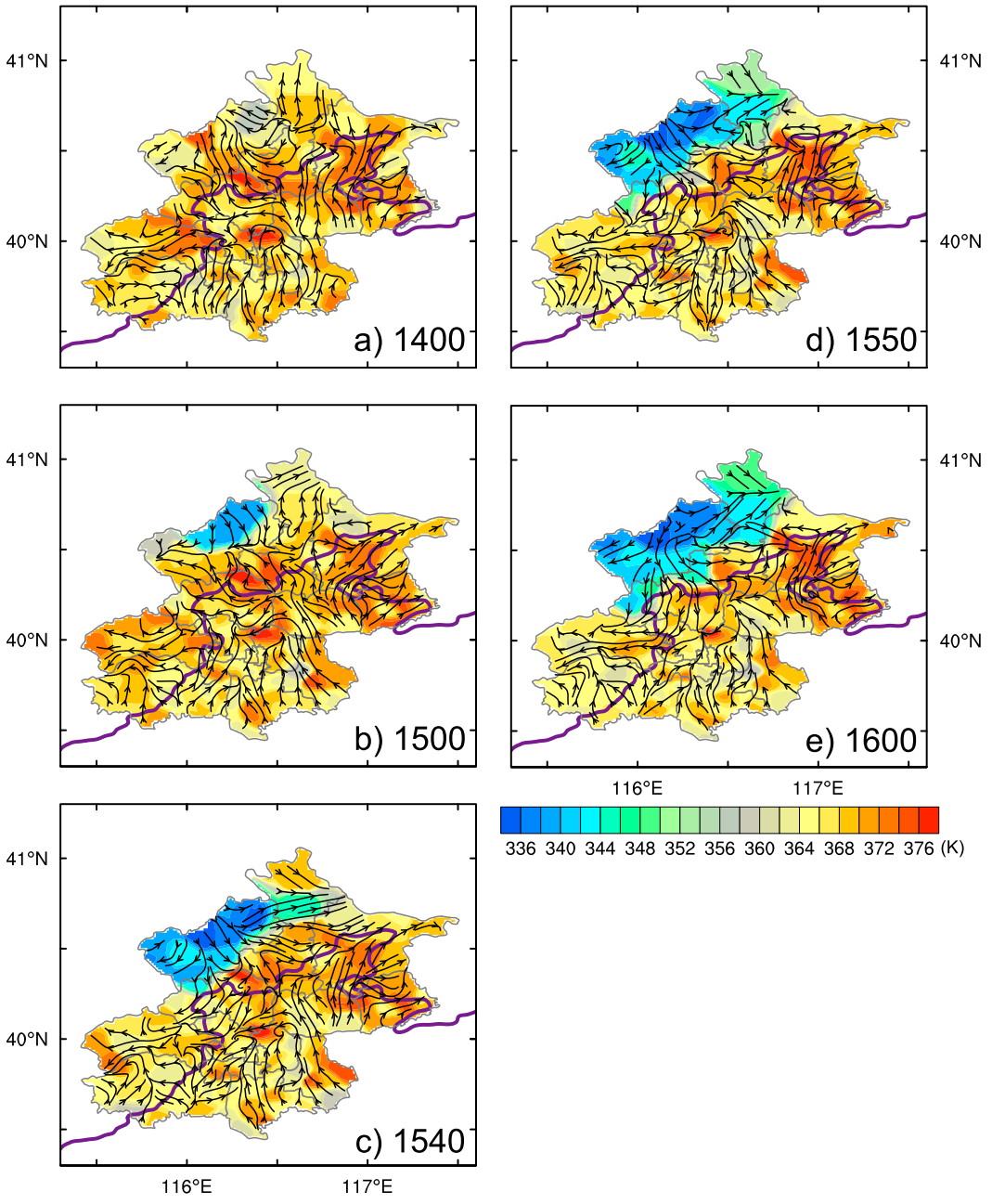

FIG. 5. Surface maps of the AWSs-observed 2-m equivalent potential temperature (θ_e in K, shaded), superimposed by 10-m surface streamlines, at (a) 1400, (b) 1500, (c) 1540, (d) 1550, and (e) 1600 LST 9 Aug 2011.

inner 1.333-km resolution domains have (x, y) dimensions of 790 × 637 and 484 × 418, respectively, covering the areas of 3160 km × 2548 km and 645.3 km × 557.3 km (see Fig. 1b for the 1.333-km resolution domain). The two domains are both integrated for 11 h from 0800 to 1900 LST 9 August 2011 using the initial and the outermost lateral boundary conditions provided by the 0.25° resolution ERA-Interim data at 6-h intervals. The following model physical schemes are used: (i) Rapid Radiative Transfer Model (RRTM) longwave radiation scheme (Mlawer et al. 1997), (ii) the Dudhia (1989) shortwave radiation scheme, (iii) the Morrison et al. (2009) double-moment microphysical parameterization, (iv) Yonsei University's PBL scheme (Hong et al. 2006), and (v) a unified Noah land surface scheme (Chen and Dudhia 2001). No cumulus parameterization scheme is used for both domains.

To improve the quality of model simulations, the four-dimensional data assimilation (FDDA) (Stauffer and

Seaman 1990; Stauffer et al. 1991; Stauffer and Seaman 1994) based on Newtonian relaxation, or the so-called nudging, is performed for both domains from 0800 to 1300 LST 9 August 2011 using surface winds, temperature, and moisture observations at hourly intervals from the BMR's AWSs network. The beginning time of free model integration (i.e., after the nudging is turned off at 1300 LST) is about 2 h prior to the propagation of the northern MCS into the BMR, and 3 h prior to the CI in HD District. Our prior numerical experimentation indicates that the dense AWS observations used during the 5-h nudging period, which is also the period of the mixed-layer development, help minimize errors between observations and the simulation, especially in the PBL over the BMR.

b. *Model verification*

Figure 6 shows the distribution of the simulated radar reflectivity beginning at 1600 LST (i.e., 3 h into the model free integration). As compared to that shown in Fig. 4, the WRF Model reproduces reasonably well the northern MCS and the convective storms to the west of MTG at 1600 LST, although the simulated MCS appears to be much weaker and displaced a little too far to the east of the observed (Fig. 6a). It is particularly encouraging that the CI location and timing of the isolated storm at the HD–CP border are well simulated (cf. Figs. 6a and 4b). Furthermore, the simulated HD storm also expands both northeastward and southwestward as in the observations (cf. Figs. 6b and 4c), and it eventually merges with the western storms to form a convective line extending from Shunyi (SY) southwestward through HD to MTG (cf. Figs. 6c and 4e), although the simulated convective line is too wide with less extensive trailing stratiform rainfall.

A comparison of Fig. 7 with Fig. 1a shows that WRF Model reproduces well the two distinct rainfall centers in southern BMR from 1600 to 1900 LST, with the locations and coverage close to the observed. The simulated rainfall amount and center in HD District are somewhat smaller and less than 25 km to the southeast of the observed, respectively. These differences are acceptable given the existing limitations in the model initial conditions and physics representations, although some differences could be attributed to the different movements of the observed and simulated storms.

The WRF Model also reproduces reasonably well the distribution of the observed high-θ_e air at 1400 LST (cf. Figs. 8a and 5a), especially with high-θ_e air in the southern CP District bordered with HD. Note, however, the presence of lower-θ_e air over the BMR's central business districts (Figs. 5 and 8), consisting of two small western and eastern districts (see Fig. 1a), which is

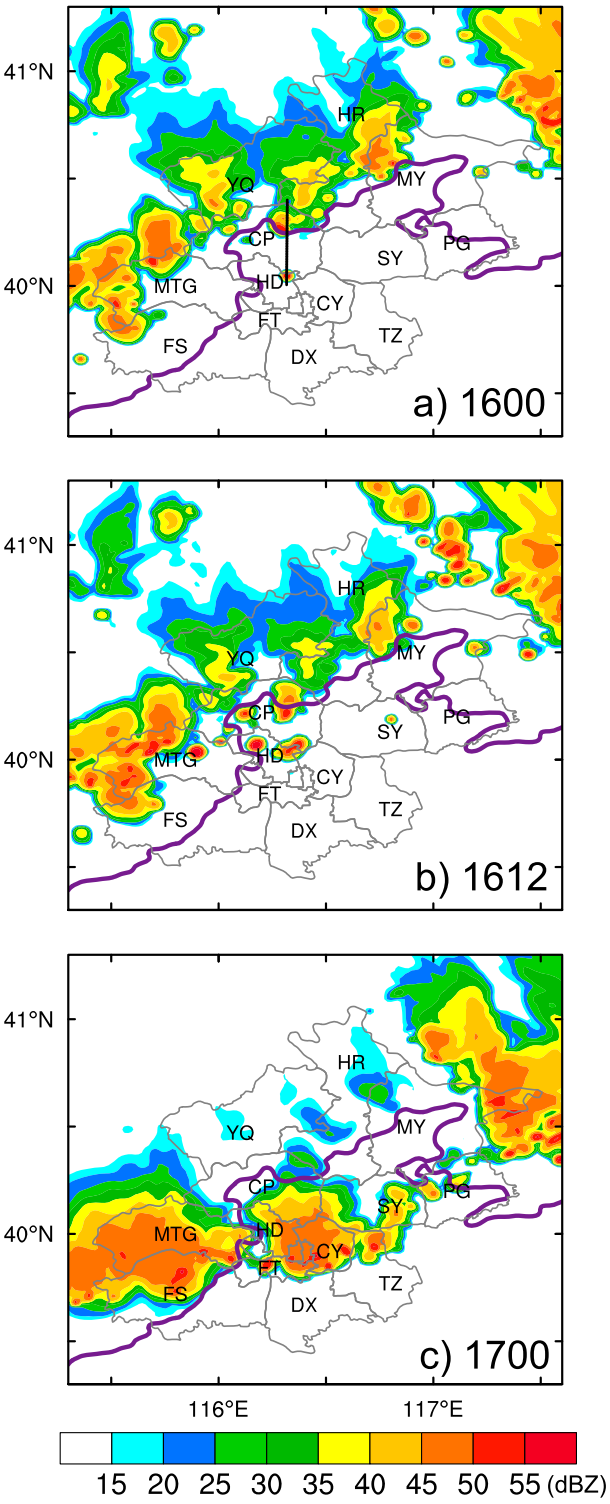

FIG. 6. As in Fig. 4, but for the simulated radar reflectivity (dBZ) at (a) 1600, (b) 1612, and (c) 1700 LST 9 Aug 2011. The black line in (a) denotes the location of vertical cross sections shown in Fig. 13.

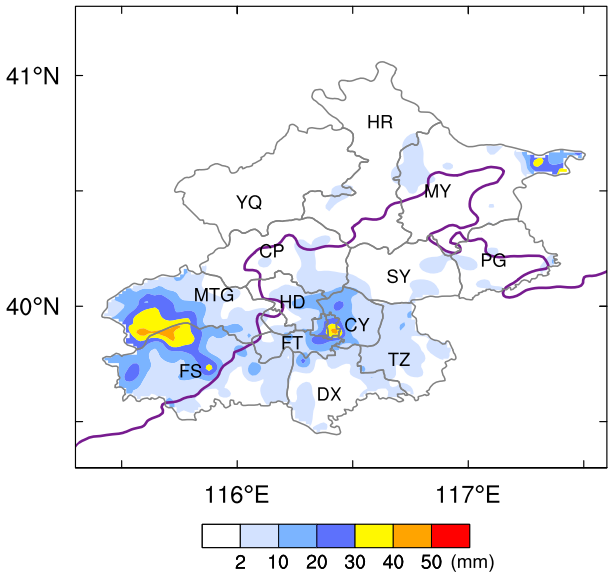

FIG. 7. As in Fig. 1a, but for the simulated 3-h accumulated precipitation (shaded, mm).

primarily caused by little evaporation of soil moisture over concrete surfaces. In fact, the model simulation shows the pronounced urban heat island (UHI) effects (Zhang et al. 2009) with surface temperature of more than 34°C over the districts, as will be shown later. A recent study of Ryu et al. (2016) shows the important roles of the UHI effects in enhancing the generation of heavy convective rainfall. The subsequent evolution of the simulated θ_e field also compares favorably to the observed, although the simulated high-θ_e areas are somewhat wider in coverage across the HD–CY–Tongzhou (TZ)–SY Districts than the observed (cf. Figs. 8b,c and 5b–d).

The model also simulates the dominant south-to-southeasterly winds over the BMR at 1400 LST as observed, including the up-valley easterly flow into the "northwestward-concaved valley" over the HD and CP Districts and a convergence area near the HD–CP border (cf. Figs. 8a and 5a). An analysis of Figs. 5 and 8 suggests that *the "northwestward-concaved" mountain shape and various surface properties contribute to locating the surface convergence center near the CI site* as they shift the direction of surface southerly flows during the daytime. Because of the wind shift, more higher-θ_e air nearby could be fed to the CI site, which may be otherwise influenced by the upstream lower-θ_e air over the BMR's central business districts. As the northern MCS enters the BMR's northwestern districts, cold outflows begin to expand southeastward. By 1548 LST, a cold outflow boundary associated with the MCS can be clearly seen along the 200-m terrain elevation contour (Fig. 8c).

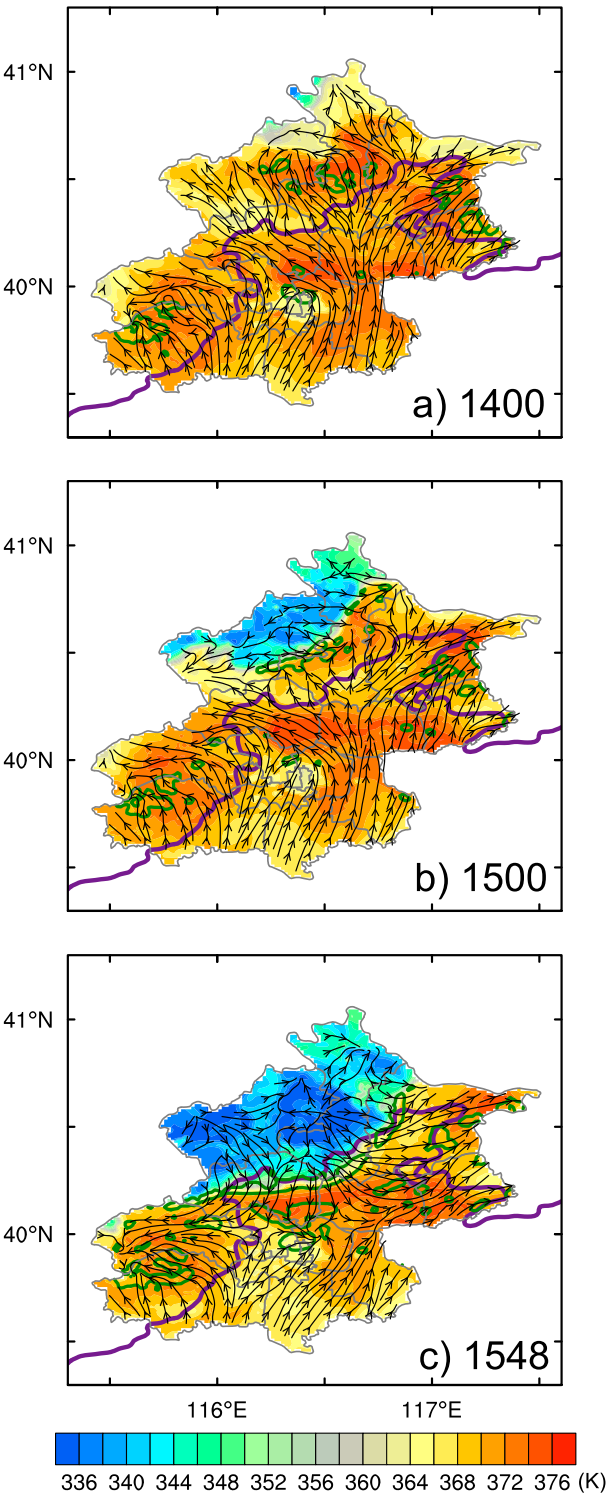

FIG. 8. As in Fig. 5, but for the simulated 2-m equivalent potential temperature (θ_e in K, shaded), superimposed by 10-m surface streamlines, at (a) 1400, (b) 1500, and (c) 1548 LST 9 Aug 2011. Green contours indicate the areas of cloud condensation in the z = 1.3–1.7-km layer (i.e., near the top of the mixed layer).

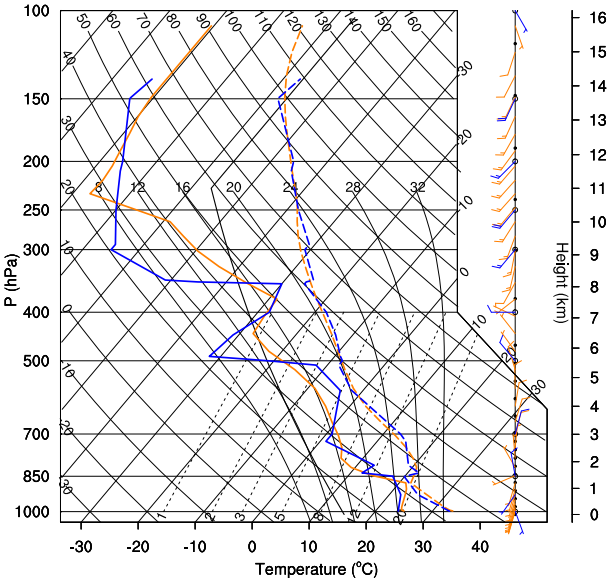

FIG. 9. Comparison of the simulated sounding (orange) to the observed (blue) at the Beijing Observatory (see Fig. 1a for its location) at 1400 LST 9 Aug 2011.

Of importance is that the WRF Model reproduces southerly flows retreating southeastward and north-to-northwesterly downslope flows advancing southeastward that converge with the south-to-southwesterly flows in the "wake" region, causing the CI of the HD storm (cf. Figs. 8c and 5c,d). Note that the simulated convergence region is less than 25 km to the southeast of the observed, which is consistent with the rainfall comparison (cf. Figs. 8b,c and 7). Moreover, the north-to-northwesterly flows advancing southeastward occur in the higher-θ_e (and also warm) air, much ahead of the cold lower-θ_e outflow boundary, as observed. Unlike the usual CI along convectively generated outflow boundaries (Wilhelmson and Chen 1982; Weckwerth and Wakimoto 1992; Wilson and Mueller 1993), the CI of the HD storm occurs far away from a cold outflow boundary.

It is of interest that while the model reproduces the development of the HD storm by 1600 LST, it also produces shallow clouds near the top of the mixed layer at several locations scattered over the higher-θ_e regions and the upsloping sides of the western and northeastern mountains, and a shallow cloud line along the leading outflow boundary during the period of 1500–1600 LST (Figs. 8b,c). Unlike the HD storm, however, few of them could develop into a precipitating system, due to the lack of sustained low-level convergence.

The simulated sounding is compared to the observed one at 1400 LST in Fig. 9, showing that the model reproduces reasonably well the observed profiles of temperature, moisture and horizontal winds, except for the sharp inversion layer near 850 hPa. This is not surprising since this time is just 1 h into the free model integration. This figure is shown here to ensure that the regional-scale environment, in which the CI of the HD storm and its heavy rain production occur, is realistically simulated, including the development of a moist and mixed PBL, conditional instability with large CAPE and a "lid" layer of CIN, and the veering of horizontal winds below 700 hPa and slow backing aloft.

In summary, despite the presence of some shortcomings in detailed features, we may state that the WRF Model captures reasonably well the spatial distribution and evolution of the major convective storms as represented by radar reflectivity and the 3-h accumulated rainfall, especially the location and timing of CI and the associated rainfall center near the HD District. Of particular relevance to the CI may be that the model reproduces the convergence region in the wake of the BMR's central business districts, the retreat of south-to-southeasterly flows and the north-to-northwesterly flows advancing southeastward much ahead of the cold outflow boundary, since the latter are closely related to the formation of an enhanced convergence region near the HD District. Given the general agreement between the simulation and observations, we may use the model output in the next section to address the questions raised in the preceding two sections.

4. Convective initiation of the HD storm

In this section, the simulation data from the 1.333-km resolution domain are used to investigate the CI processes leading to the formation of the isolated HD storm. Let us examine first when and what layer gridbox saturation denoting the CI is initiated. For this purpose, Fig. 10 shows the simulated soundings at 1400 and 1548 LST at the CI location. As shown in Fig. 3, the BMR's lower troposphere in the early morning was characterized by a stable layer below 850 hPa that was capped by a dry layer up to 600 hPa. As the surface layer was heated, a well-mixed layer developed in the early afternoon. A comparison of the 1400 LST soundings in Figs. 9 and 10 indicates that the mixed layer at the CI site is more humid (i.e., with the specific humidity of 20–21 g kg^{-1}) than those at the BMR's observatory site (i.e., with the specific humidity of 19–20 g kg^{-1}), which are consistent with the presence of high-θ_e air shown in Fig. 5a. As a result, the mixed-layer top (near 875 hPa) at the CI site is closer to saturation at 1400 LST due to the mixed-layer development aided likely by convergence in the PBL. However, free convective overturning is not possible, because of the presence of some CIN in a 1-km lid layer at the top of the mixed layer.

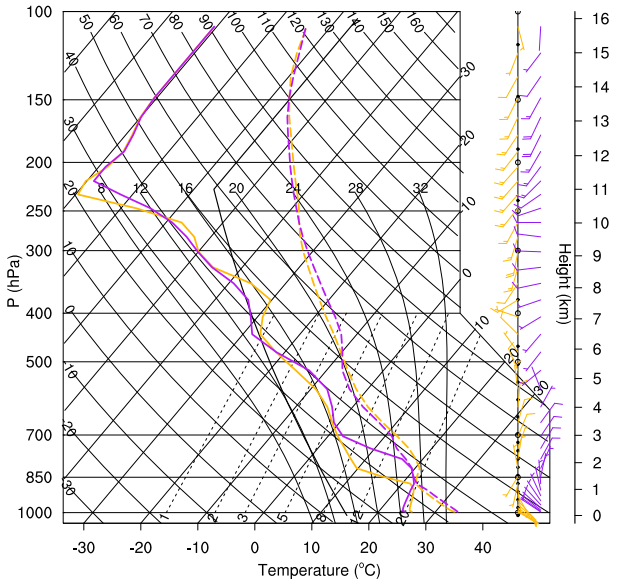

FIG. 10. Simulated soundings at the CI location at 1400 (gold) and 1548 (purple) LST 9 Aug 2011.

By 1548 LST (i.e., just 12 min prior to the emergence of a distinct radar echo associated with the HD storm) (Figs. 6a and 4b), the CIN in the stable layer has been overcome by an ascending air parcel, forced by latent heat release, that is initiated with the saturated temperature and mixing ratio at the top of the mixed layer. As a result, a 1.2-km saturated layer with a moist-adiabatic lapse rate is generated, implying the formation of clouds. In particular, this sounding now becomes absolutely unstable, suggesting the development of robust updrafts without any further needed uplifting. In fact, the dewpoint depression above the saturated layer and below 700 hPa has decreased significantly as a result of the upward penetration of buoyancy-driven updrafts, given the presence of large CAPE.

To illustrate the CI processes in more detail, Fig. 11 shows the time–height cross sections of several variables, including temperature and specific humidity deviations from their values at 1400 LST, cloud water and rainwater, divergence and vertical motion, as well as horizontal winds, at the CI location. It is evident that the mixed layer still keeps warming and drying, while upward detrainment of free convective eddies into the stable layer above causes local cooling and moistening in a 600-m-layer centered at $z = 1.5$ km, until 1512 LST when a shallow layer of clouds begins to form as a result of gridbox saturation in the detaining layer. This thermodynamic structural changes are of typical mixed-layer development (Hong et al. 2006; Zhang and Anthes 1982), but herein enhanced by the respective convergence and divergence in the mixed and detrainment layer in excess of $5 \times 10^{-4}\,s^{-1}$ after 1430 LST (Fig. 11b). Ziegler and Rasmussen (1998) showed that the depth and intensity of convergence and updraft rather than the surface convergence alone played a pivotal role in the initiation of deep convection. As can be seen in Fig. 11b, the convergence gradually grew deeper and stronger after 1512 LST. It takes about 36 min for the condensation-driven updrafts to remove the CIN in the lid layer above, before convective outbreak with intense updrafts occurs at 1548 LST (cf. Figs. 11a,b and 10). The lowest PBL begins to experience cooling as a result of evaporation of rainwater shortly after the convective outbreak, and the subsequent growth of the HD storm is driven by latent heat release, and moisture convergence, especially energy supply from the southerly warm and moist air current.

Note that the horizontal winds in the lowest 1-km layer turn anticyclonically (i.e., from south-southeasterly prior to 1500 LST to westerly at 1536 LST and northwesterly at 1548 LST) experiencing the typical inertial oscillation in the PBL (Blackadar 1957; Zhang and Zheng 2004), while they remain northeasterly with little changes in speed and direction above $z = 1.8$ km at the CI location (Fig. 11c). This inertial oscillation is interrupted after 1548 LST, with the increasing horizontal wind speeds from less than $2\,m\,s^{-1}$ before to greater than $6\,m\,s^{-1}$ at 1612 LST. A comparison between Figs. 8 and 5 shows that such changes in wind speed and direction represent the evolution of horizontal winds near the HD storm from the dominant prestorm environmental winds (Fig. 8b) to the convectively forced flows (Fig. 8c) and the intrusion of the northerly winds (Figs. 8c and 5d,e).

Of interest is the development of the northerly flow that appears first at about 1-km altitude at 1536 LST (i.e., about 24 min after the cloud formation at the PBL top) (cf. Figs. 11a,c), and then extends to the surface layer by 1600 LST (cf. Figs. 11c and 8b,c). Since this northerly flow is shown earlier to converge with the southerly warm/moist air for the formation of the HD storm, it is desirable to investigate how it develops. First, the latent heating–induced convergence must account for the earlier northerly flow near the PBL top and its subsequent increase in speed and downward extension. Figure 12, showing a pressure perturbation field from a domain mean at $z = 0.5$ km after applying the pressure reduction, indicates that a well-defined meso-β-scale high, collocated with a surface cold dome in northeastern YQ that is generated by the northern MCS (cf. Figs. 12a and 8b), also contributes to the enhancement of the northerly flow, at least, at later stages. Specifically, cold outflows associated the convectively generated cold dome expand rapidly southwestward, but slowly southeastward due to different terrain (cf. Figs. 5 and 8). Downslope outflows begin to emerge in the warm air

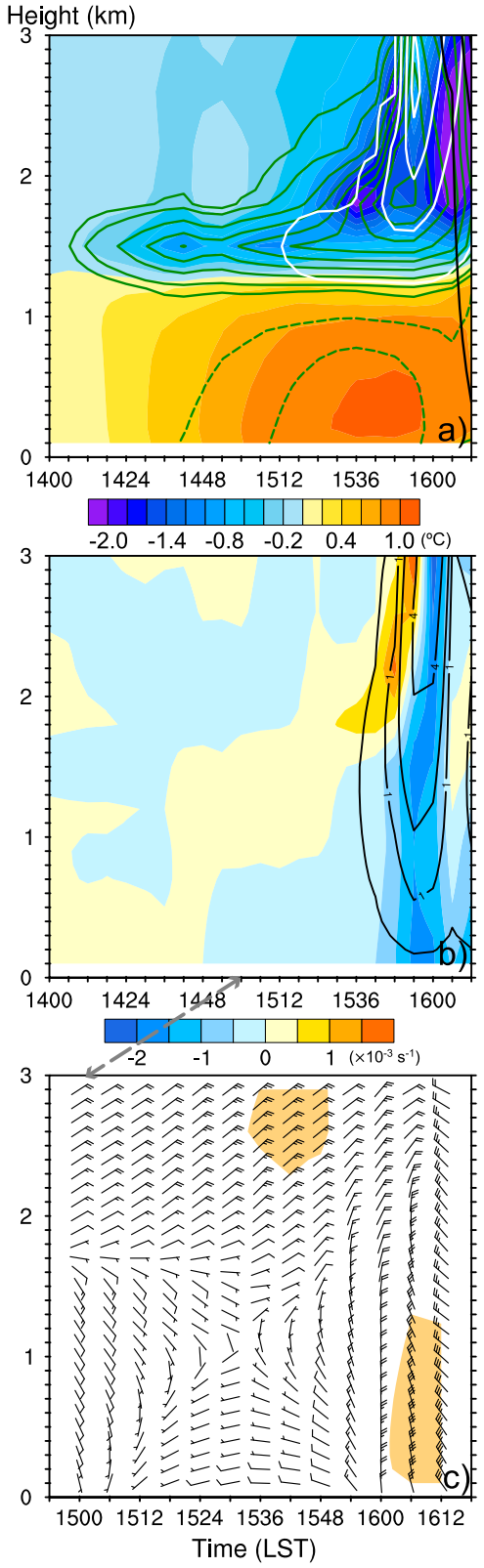

FIG. 11. Time–height plots of (a) temperature deviations (shaded, °C), specific humidity deviations (contoured in green, dashed for -1, $-0.5\,\mathrm{g\,kg^{-1}}$, and solid for 0.5, 1, 2, 3, . . . , $\mathrm{g\,kg^{-1}}$), cloud water (contoured in white, starting at $0.05\,\mathrm{g\,kg^{-1}}$ at intervals of $0.5\,\mathrm{g\,kg^{-1}}$), and rainwater (contoured in black, starting at $0.05\,\mathrm{g\,kg^{-1}}$ at intervals of $0.5\,\mathrm{g\,kg^{-1}}$), where the temperature and specific humidity deviations are defined as differences from their values at 1400 LST; (b) divergence (shaded, $10^{-3}\,\mathrm{s^{-1}}$) and vertical velocity (contoured in black at $0.25 \times 2^N\,\mathrm{m\,s^{-1}}$, where $N = 0, 1, 2, 3, \ldots$); and (c) horizontal winds (a full barb is $2\,\mathrm{m\,s^{-1}}$), with the wind speeds greater than $5\,\mathrm{m\,s^{-1}}$ shaded. All the vertical profiles are averaged over an area of 4 km × 4 km centered at the CI location. Note that the starting time in (a) and (b) is 1400 LST but 1500 LST in (c) [indicated by dashed arrow between (b) and (c)], since the horizontal winds at the CI location change little between 1400 and 1500 LST.

ahead of the cold outflow boundary at 1518 LST (Fig. 12b). Like the density current, the divergent outflows in the warm air, increasing downward in the PBL shown in Fig. 13d, appear to be driven by the pressure gradient force associated with the mesohigh. Note that this warm northerly "outflow" of less than $2\,\mathrm{m\,s^{-1}}$ would become a southerly inflow in a reference frame with respect to the cold outflow boundary. As the cold pool and mesohigh expand southward, the northerly outflow approaches the northern HD District, increasing the local convergence or the confluence of streamlines at the CI site (Figs. 12c–f).

By comparison, the western MCS, which is still located over the western mountains of the MTG District, does not produce a distinct surface cold pool over MTG and FS, so meso-β-scale lows appear there. The pressure perturbations of different signs over MTG and FS from those over YQ and HR associated with the northern MCS might be attributed to their different development stages and the presence of different midtropospheric conditions. Namely, storms in their early development stages might have not yet produced enough cold air mass. A relatively warm and moist midtroposphere from the south tends to induce weaker and less cold moist downdrafts than a cold and dry one from the north. The above results suggest that the northern MCS propagating eastward with a distance of about 50 km away, assists to some degree in the CI of the HD storm, whereas the western MCS does not, because of lacking convectively generated cold pools. Nevertheless, as the western MCS moves eastward, it produces cold outflows, which interact with the HD storm, thus contributing to the subsequent generation of heavy rainfall near HD (Figs. 6 and 7).

Figure 13 describes the south–north vertical cross-sectional evolution through the CI site of the processes leading to the convective outbreak of the HD storm. At the time of cloud water formation in a thin layer centered at $z = 1.5$ km (Fig. 13a), we see little convergence and upward motion immediately underneath, except in the lowest 800-m layer, but a high-θ_e or warm bubble in

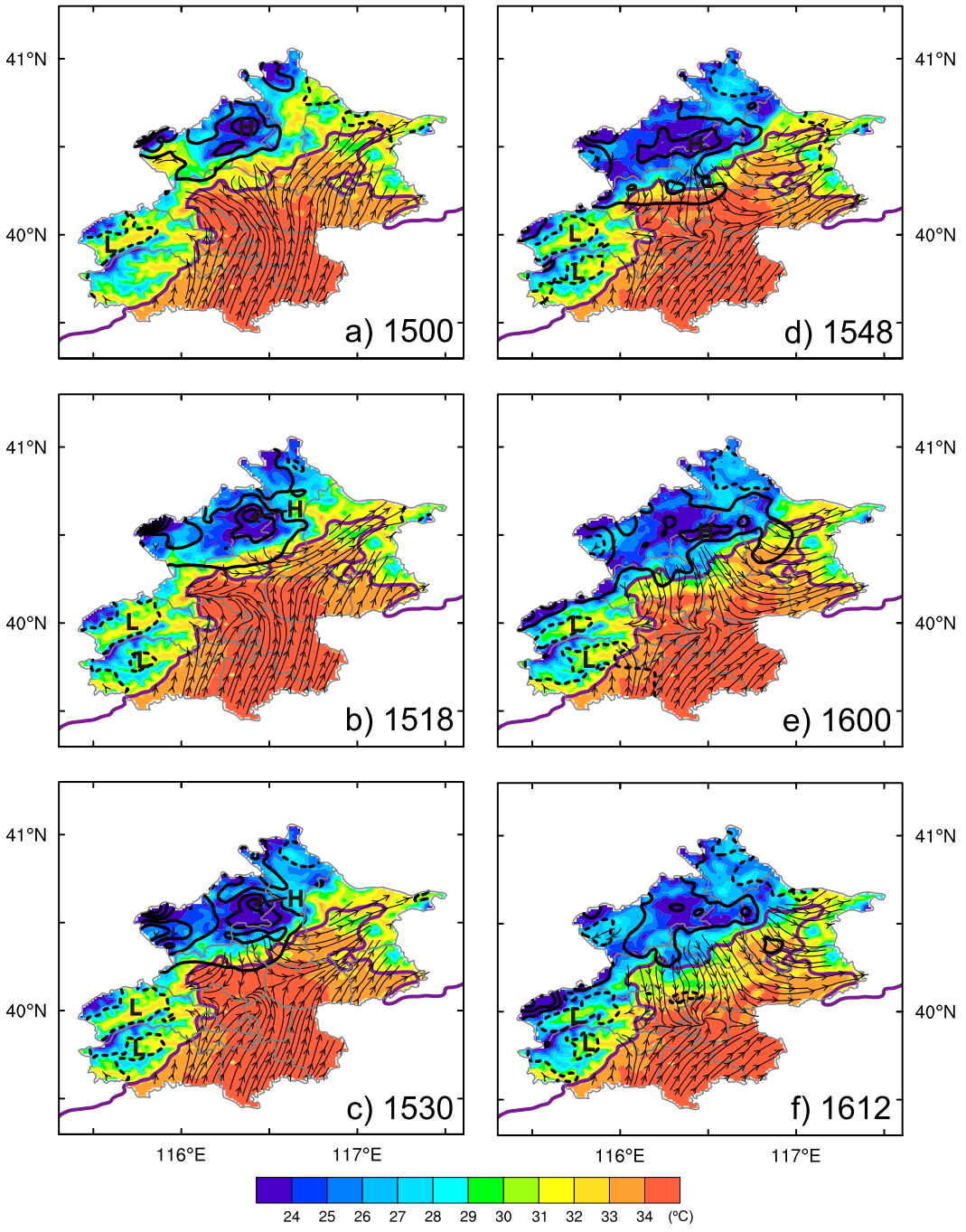

FIG. 12. Pressure perturbations from the domain mean (contoured in thick black, solid/positive and dashed/negative, starting from ±0.5 hPa at 1-hPa intervals), 2-m surface temperature (shaded, °C), superimposed with streamlines, at $z = 0.5$ km MSL at (a) 1500, (b) 1518, (c) 1530, (d) 1548, (e) 1600, and 1612 LST 9 Aug 2011. Letters, "H" and "L" denote the center of a mesohigh and a mesolow, respectively.

the lowest 600-m layer, as also indicated in Figs. 8b, 11a, and 12, and an elevated mixed layer, as denoted by high-θ_e layers. Clearly, this shallow layer of local cloud condensation is initiated with little influences from convectively generated perturbations associated the northern MCS (and western MCS); similarly for the scattered PBL clouds elsewhere over the BMR as shown in Fig. 8. Thus, we may state that the CI of the HD storm occurs first from the mixed-layer development associated with the UHI effects of the BMR's central business districts.

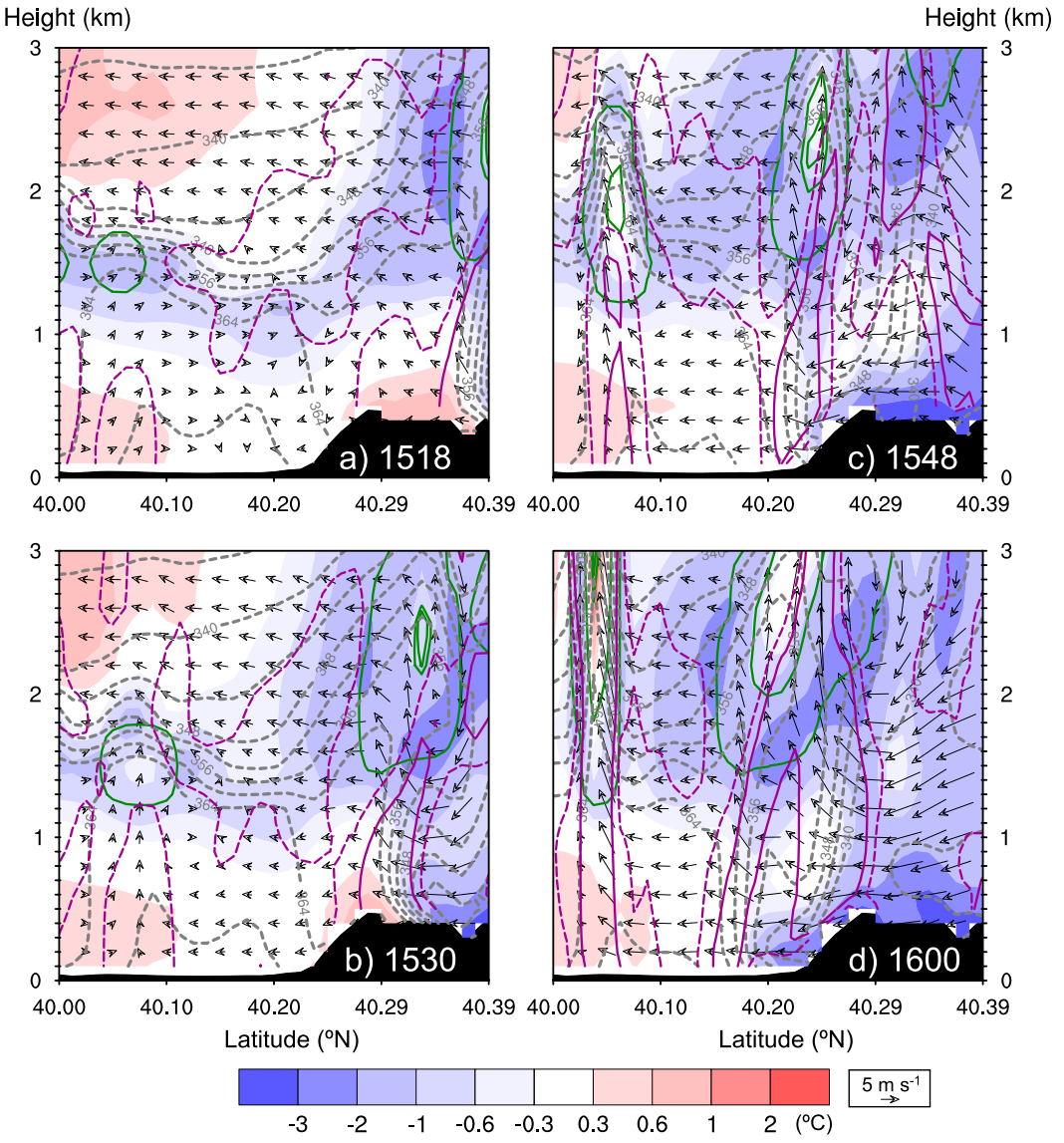

FIG. 13. Vertical cross sections along the line given in Fig. 6a, east–west averaged over a 4-km width, of temperature perturbations from their level-averaged values (shaded, °C), equivalent potential temperature (θ_e, contoured in dashed gray at intervals of 4K), cloud water (contoured in green starting at 0.05 g kg^{-1} at intervals of 1 g kg^{-1}), divergence (dashed and solid magenta contours for -10^{-4} and -10^{-3} s^{-1}, respectively), superimposed with in-plane flow vectors with vertical motion amplified by a factor of 5 at (a) 1518, (b) 1530, (c) 1548, and 1600 LST 9 Aug 2011. Terrain is shaded in black.

The latent heat release from the cloud formation induces immediately favorable convergence of the northerly and southerly flows, albeit weak, and upward motion in the entire PBL depth. Meanwhile, the divergent northerly flow resulting from a mesohigh region associated with the northern MCS increases in amplitude from 1.5-km altitude downward, and triggers cloud condensation above the PBL ahead of the leading θ_e front (Figs. 13a–c). The characteristics of the downward-increased northerly flow become evident near the CI site at 1600 LST when the θ_e front moves from the mountainous regions down to the plains (Fig. 13d). This gives the timing of the influences of the northern MCS, through the low-level northerly flow driven by the mesohigh, on the subsequent growth of the HD storm.

5. Summary and conclusions

In this study, the CI of an isolated heavy-rain-producing thunderstorm near the BMR's central urban area (i.e., HD

District) on 9 August 2011 is examined in order to understand the impact of the UHI effects, mountain morphology, and other factors on the generation of isolated heavy rainfall events in the BMR during the summer months. An observational analysis of the ECMWF reanalysis, upper-air soundings and AWSs data shows that the large-scale quasigeostrophic conditions for the present case were unfavorable for organized convective development, but the regional environment was favorable for CI, including the presence of conditional instability, a low-level southerly flow with weak warm advection and a high-θ_e tongue. The isolated storm was initiated at some distance from BMR's northwestern mountains and two preexisting MCSs to the west and north, respectively.

A cloud-resolving simulation of the case is performed to study the processes leading to the CI of the HD storm. Results show that the HD storm begins with a thin layer of cloud condensation at the top of the urban boundary layer, as a result of the afternoon development of the mixed layer, aided by the UHI effects over the BMR's central business districts. The boundary layer top cloud condensation also occurs elsewhere, scattered over higher-θ_e areas and on the upslope sides of the BMR's mountainous regions during the late afternoon hours. Both the AWSs data and the model simulation indicate that up-valley flows into the northwestward-concaved valleys in the BMR's western mountains shift the incoming southerly flow, forming a favorable convergence area near the HD–CP border. This wind shift would then allow more higher-θ_e air nearby to be fed to the CI site, which may be otherwise influenced by the upstream lower-θ_e air over the BMR's central business districts. It takes about 36 min for the condensation-driven updrafts to remove a 1-km layer of CIN above the mixed layer before the occurrence of convective outbreak with intense updrafts. However, this isolated convective outbreak would not be possible without the sustained low-level convergence of high-θ_e air between south-to-southeasterly flows and a northerly flow. The latter occurs far ahead of a meso-β-scale high associated with a convectively generated cold pool by the northern MCS. Figure 14 provides a schematic description of the above processes.

In conclusion, we may state that the daytime mixed-layer development, enhanced by the UHI effects, accounts for the generation of shallow clouds at the top of the mixed layer. The up-valley flows into the northwestward-concaved valleys in the BMR's western mountains shift the incoming southerly flow westward (orange arrows in Fig. 14) to facilitate the formation of a favorable convergence area near the HD–CP border and the subsequent supply of high-θ_e air for the CI of the HD storm. However, it appears to be the sustained low-level convergence of the south-to-southeasterly flows with the northerly flow (thick blue arrows in Fig. 14) driven more by the latent heating of the formed shallow cloud condensation during the earlier CI stages, and by a mesohigh (gray contours in Fig. 14) associated with the northern MCS during the later CI stages of the HD storm. In our forthcoming study, a series of sensitivity experiments will be performed to further examine the roles of the UHI effects, surface roughness, possible "blocking" effects of high buildings in the BMR's central business districts, mountain morphology, and convective interaction in determining the CI timing and location of isolated heavy-rain-producing thunderstorms in the BMR.

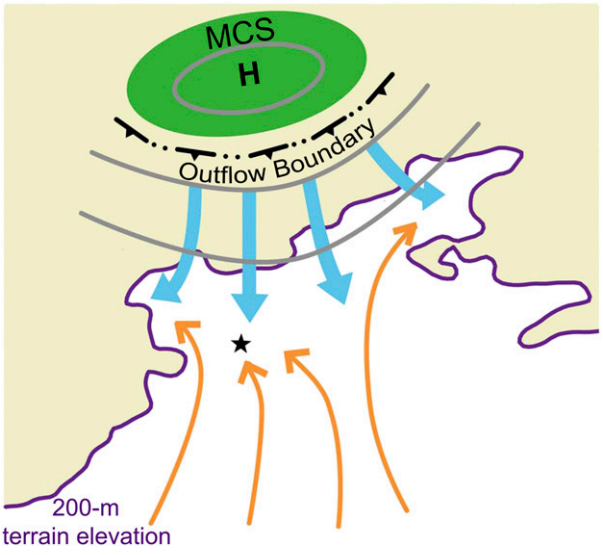

FIG. 14. Schematic diagram of various flows influencing the CI of the HD storm. The star marks the CI location. Orange arrows indicate the surface southerly flow. Thick blue arrows indicate the northerly flow associated with a convectively generated mesohigh depicted by gray contours. Yellow shadings denote the mountainous regions.

Acknowledgments. This work was supported by the National Basic Research Program of China (973 Program) under Grant 2014CB441402. The authors are grateful to the European Centre for Medium-Range Weather Forecasts (ECMWF) for providing ERA-Interim data (http://apps.ecmwf.int/datasets/data/interim-full-daily/) and to Beijing Meteorological Bureau for providing observational data in Beijing. The authors also wish to thank the two anonymous reviewers for their constructive comments on this paper. The model simulations were performed on TianHe-1 (A) at National Supercomputer Center in Tianjin, China.

REFERENCES

Baker, R. D., B. H. Lynn, A. Boone, W.-K. Tao, and J. Simpson, 2001: The influence of soil moisture, coastline curvature, and land-breeze circulations on sea-breeze-initiated precipitation. *J. Hydrometeor.*, **2**, 193–211, doi:10.1175/1525-7541(2001)002<0193:TIOSMC>2.0.CO;2.

Behrendt, A., and Coauthors, 2011: Observation of convection initiation processes with a suite of state-of-the-art research instruments during COPS IOP 8b. *Quart. J. Roy. Meteor. Soc.*, **137**, 81–100, doi:10.1002/qj.758.

Blackadar, A. K., 1957: Boundary layer wind maxima and their significance for the growth of nocturnal inversions. *Bull. Amer. Meteor. Soc.*, **83**, 283–290.

Browning, K. A., and Coauthors, 2007: The Convective Storm Initiation Project. *Bull. Amer. Meteor. Soc.*, **88**, 1939–1955, doi:10.1175/BAMS-88-12-1939.

Byers, H. R., and H. R. Rodebush, 1948: Causes of thunderstorms of the Florida Peninsula. *J. Meteor.*, **5**, 275–280, doi:10.1175/1520-0469(1948)005<0275:COTOTF>2.0.CO;2.

Chen, F., and J. Dudhia, 2001: Coupling an advanced land surface-hydrology model with the Penn State–NCAR MM5 modeling system. Part I: Model description and implementation. *Mon. Wea. Rev.*, **129**, 569–585, doi:10.1175/1520-0493(2001)129<0569:CAALSH>2.0.CO;2.

Clark, C. A., and R. W. Arritt, 1995: Numerical simulations of the effect of soil moisture and vegetation cover on the development of deep convection. *J. Appl. Meteor.*, **34**, 2029–2045, doi:10.1175/1520-0450(1995)034<2029:NSOTEO>2.0.CO;2.

Dudhia, J., 1989: Numerical study of convection observed during the winter monsoon experiment using a mesoscale two-dimensional model. *J. Atmos. Sci.*, **46**, 3077–3107, doi:10.1175/1520-0469(1989)046<3077:NSOCOD>2.0.CO;2.

Hane, C. E., C. L. Ziegler, and H. B. Bluestein, 1993: Investigation of the dryline and convective storms initiated along the dryline: Field experiments during COPS-91. *Bull. Amer. Meteor. Soc.*, **74**, 2133–2145, doi:10.1175/1520-0477(1993)074<2133:IOTDAC>2.0.CO;2.

Hong, S.-Y., Y. Noh, and J. Dudhia, 2006: A new vertical diffusion package with an explicit treatment of entrainment processes. *Mon. Wea. Rev.*, **134**, 2318–2341, doi:10.1175/MWR3199.1.

Kain, J. S., and J. M. Fritsch, 1992: The role of the convective ''trigger function'' in numerical forecasts of mesoscale convective systems. *Meteor. Atmos. Phys.*, **49**, 93–106, doi:10.1007/BF01025402.

Khairoutdinov, M., and D. Randall, 2006: High-resolution simulation of shallow-to-deep convection transition over land. *J. Atmos. Sci.*, **63**, 3421–3436, doi:10.1175/JAS3810.1.

Koch, S. E., and C. A. Ray, 1997: Mesoanalysis of summertime convergence zones in central and eastern North Carolina. *Wea. Forecasting*, **12**, 56–77, doi:10.1175/1520-0434(1997)012<0056:MOSCZI>2.0.CO;2.

Lean, H. W., N. M. Roberts, P. A. Clark, and C. Morcrette, 2009: The surprising role of orography in the initiation of an isolated thunderstorm in southern England. *Mon. Wea. Rev.*, **137**, 3026–3046, doi:10.1175/2009MWR2743.1.

Lima, M. A., and J. W. Wilson, 2008: Convective storm initiation in a moist tropical environment. *Mon. Wea. Rev.*, **136**, 1847–1864, doi:10.1175/2007MWR2279.1.

Lin, Y.-L., S. Chiao, T.-A. Wang, M. L. Kaplan, and R. P. Weglarz, 2001: Some common ingredients for heavy orographic rainfall. *Wea. Forecasting*, **16**, 633–660, doi:10.1175/1520-0434(2001)016<0633:SCIFHO>2.0.CO;2.

Mlawer, E. J., S. J. Taubman, P. D. Brown, M. J. Iacono, and S. A. Clough, 1997: Radiative transfer for inhomogeneous atmosphere: RRTM, a validated correlated-k model for the long-wave. *J. Geophys. Res.*, **102**, 16 663–16 682, doi:10.1029/97JD00237.

Morrison, H., G. Thompson, and V. Tatarskii, 2009: Impact of cloud microphysics on the development of trailing stratiform precipitation in a simulated squall line: Comparison of one- and two-moment schemes. *Mon. Wea. Rev.*, **137**, 991–1007, doi:10.1175/2008MWR2556.1.

Mueller, C. K., J. W. Wilson, and N. A. Crook, 1993: The utility of sounding and mesonet data to nowcast thunderstorm initiation. *Wea. Forecasting*, **8**, 132–146, doi:10.1175/1520-0434(1993)008<0132:TUOSAM>2.0.CO;2.

Murphey, H. V., R. M. Wakimoto, C. Flamant, and D. E. Kingsmill, 2006: Dryline on 19 June 2002 during IHOP. Part I: Airborne Doppler and LEANDRE II analyses of the thin line structure and convection initiation. *Mon. Wea. Rev.*, **134**, 406–430, doi:10.1175/MWR3063.1.

Purdom, J. F. W., 1976: Some uses of high resolution GOES imagery in the mesoscale forecasting of convection and its behavior. *Mon. Wea. Rev.*, **104**, 1474–1483, doi:10.1175/1520-0493(1976)104<1474:SUOHRG>2.0.CO;2.

Rhea, J. O., 1966: A study of thunderstorm formation along dry lines. *J. Appl. Meteor.*, **5**, 58–63, doi:10.1175/1520-0450(1966)005<0058:ASOTFA>2.0.CO;2.

Ryu, Y.-H., J. A. Smith, E. Bou-Zeid, and M. L. Baeck, 2016: The influence of land surface heterogeneities on heavy convective rainfall in the Baltimore–Washington metropolitan area. *Mon. Wea. Rev.*, **144**, 553–573, doi:10.1175/MWR-D-15-0192.1.

Skamarock, W. C., and Coauthors, 2008: A description of the Advanced Research WRF version 3. NCAR Tech. Note NCAR/TN-475+STR, 113 pp., doi:10.5065/D68S4MVH.

Stauffer, D. R., and N. L. Seaman, 1990: Use of four-dimensional data assimilation in a limited-area mesoscale model. Part I: Experiments with synoptic-scale data. *Mon. Wea. Rev.*, **118**, 1250–1277, doi:10.1175/1520-0493(1990)118<1250:UOFDDA>2.0.CO;2.

——, and ——, 1994: Multiscale four-dimensional data assimilation. *J. Appl. Meteor.*, **33**, 416–434, doi:10.1175/1520-0450(1994)033<0416:MFDDA>2.0.CO;2.

——, ——, and F. S. Binkowski, 1991: Use of four-dimensional data assimilation in a limited-area mesoscale model. Part II: Effects of data assimilation within the planetary boundary layer. *Mon. Wea. Rev.*, **119**, 734–754, doi:10.1175/1520-0493(1991)119<0734:UOFDDA>2.0.CO;2.

Van Baelen, J., M. Reverdy, F. Tridon, L. Labbouz, G. Dick, M. Bender, and M. Hagen, 2011: On the relationship between water vapour field evolution and the life cycle of precipitation systems. *Quart. J. Roy. Meteor. Soc.*, **137**, 204–223, doi:10.1002/qj.785.

Wang, H., and J.-S. Sun, 2008: Effects of underlying surface physical process on a severe hail event occurred in Beijing area (in Chinese with an English abstract). *Meteor. Mon.*, **34**, 16–21.

Wang, Q.-W., and M. Xue, 2012: Convective initiation on 19 June 2002 during IHOP: High-resolution simulations and analysis of the mesoscale structures and convection initiation. *J. Geophys. Res.*, **117**, D12107, doi:10.1029/2012JD017552.

Wang, T., Y. Wang, M. Chen, and W. Zhang, 2011: The contrastive analysis of formation of dry and moist convective storms in Beijing (in Chinese with an English abstract). *Meteor. Mon.*, **37**, 142–155.

Weckwerth, T. M., 2000: The effect of small-scale moisture variability on thunderstorm initiation. *Mon. Wea. Rev.*, **128**, 4017–4030, doi:10.1175/1520-0493(2000)129<4017:TEOSSM>2.0.CO;2.

——, and R. M. Wakimoto, 1992: The initiation and organization of convective cells atop a cloud-air outflow boundary. *Mon. Wea. Rev.*, **120**, 2169–2187, doi:10.1175/1520-0493(1992)120<2169:TIAOOC>2.0.CO;2.

——, J. W. Wilson, and R. M. Wakimoto, 1996: Thermodynamic variability within the convective boundary layer due to horizontal convective rolls. *Mon. Wea. Rev.*, **124**, 769–784, doi:10.1175/1520-0493(1996)124<0769:TVWTCB>2.0.CO;2.

——, and Coauthors, 2004: An overview of the International H_2O Project (IHOP_2002) and some preliminary highlights. *Bull. Amer. Meteor. Soc.*, **85**, 253–277, doi:10.1175/BAMS-85-2-253.

——, L. J. Bennett, L. J. Miller, J. Van Baelen, P. Di Girolamo, A. M. Blyth, and T. J. Hertneky, 2014: An observational and modeling study of the processes leading to deep, moist convection in complex terrain. *Mon. Wea. Rev.*, **142**, 2687–2708, doi:10.1175/MWR-D-13-00216.1.

Whiteman, C. D., 2000: *Mountain Meteorology*. Oxford University Press, 355 pp.

Wilhelmson, R. B., and C.-S. Chen, 1982: A simulation of the development of successive cells along a cold outflow boundary. *J. Atmos. Sci.*, **39**, 1466–1483, doi:10.1175/1520-0469(1982)039<1466:ASOTDO>2.0.CO;2.

Wilson, J. W., and W. E. Schreiber, 1986: Initiation of convective storms at radar-observed boundary-layer convergence lines. *Mon. Wea. Rev.*, **114**, 2516–2536, doi:10.1175/1520-0493(1986)114<2516:IOCSAR>2.0.CO;2.

——, and C. K. Mueller, 1993: Nowcasts of thunderstorm initiation and evolution. *Wea. Forecasting*, **8**, 113–131, doi:10.1175/1520-0434(1993)008<0113:NOTIAE>2.0.CO;2.

——, and D. L. Megenhardt, 1997: Thunderstorm initiation, organization, and lifetime associated with Florida boundary layer convergence lines. *Mon. Wea. Rev.*, **125**, 1507–1525, doi:10.1175/1520-0493(1997)125<1507:TIOALA>2.0.CO;2.

——, J. A. Moore, G. B. Foote, B. Martner, T. Uttal, J. M. Wilczak, and A. R. Rodi, 1988: Convective Initiation and Downburst Experiment (CINDE). *Bull. Amer. Meteor. Soc.*, **69**, 1328–1348, doi:10.1175/1520-0477(1988)069<1328:CIADE>2.0.CO;2.

——, G. B. Foote, N. A. Crook, J. C. Fankhauser, C. G. Wade, J. D. Tuttle, C. K. Mueller, and S. K. Krueger, 1992: The role of boundary-layer convergence zones and horizontal rolls in the initiation of thunderstorms: A case study. *Mon. Wea. Rev.*, **120**, 1785–1815, doi:10.1175/1520-0493(1992)120<1785:TROBLC>2.0.CO;2.

——, Y. Feng, M. Chen, and R. D. Roberts, 2010: Nowcasting challenges during the Beijing Olympics: Successes, failures, and implications for future nowcasting systems. *Wea. Forecasting*, **25**, 1691–1714, doi:10.1175/2010WAF2222417.1.

Wulfmeyer, V., and Coauthors, 2008: The Convective and Orographically Induced Precipitation Study: A research and development project of the World Weather Research Program for improving quantitative precipitation forecasting in low-mountain regions. *Bull. Amer. Meteor. Soc.*, **89**, 1477–1486, doi:10.1175/2008BAMS2367.1.

Xiao, X., M. Chen, F. Gao, and Y. Wang, 2015: A thermodynamic mechanism analysis on enhancement of dissipation of convective systems from the mountains under weak synoptic forcing (in Chinese with an English abstact). *Chin. J. Atmos. Sci.*, **39**, 100–124.

Zhang, D.-L., and R. A. Anthes, 1982: A high-resolution model of the planetary boundary layer—Sensitivity tests and comparisons with SESAME-79 data. *J. Appl. Meteor.*, **21**, 1594–1609, doi:10.1175/1520-0450(1982)021<1594:AHRMOT>2.0.CO;2.

——, and J. M. Fritsch, 1986: Numerical simulation of the meso-β scale structure and evolution of the 1977 Johnstown flood. Part I: Model description and verification. *J. Atmos. Sci.*, **43**, 1913–1943, doi:10.1175/1520-0469(1986)043<1913:NSOTMS>2.0.CO;2.

——, and W. Zheng, 2004: Diurnal cycles of surface winds and temperatures as simulated by five boundary-layer parameterizations. *J. Appl. Meteor.*, **43**, 157–169, doi:10.1175/1520-0450(2004)043<0157:DCOSWA>2.0.CO;2.

——, Y.-X. Shou, and R. R. Dickerson, 2009: Upstream urbanization exacerbates urban heat island effects. *Geophys. Res. Lett.*, **36**, L24401, doi:10.1029/2009GL041082.

Zhang, W., Y. Wang, X. Cui, and T. Wang, 2011: Comparative analysis on numerical test between dry convective storm and moist convective storm in Beijing (in Chinese with an English abstract). *Torrential Rain Disaster*, **30**, 202–209.

——, X. Cui, Y. Wang, Q. Li, and R. Huang, 2013: Roles of low-level easterly winds in the local torrential rains of Beijing (in Chinese with an English abstract). *Chin. J. Atmos. Sci.*, **37**, 829–840.

——, ——, and R. Huang, 2014: Intensive observational study on evolution of formation location of convective storms in Beijing under complex topographical conditions (in Chinese with an English abstract). *Chin. J. Atmos. Sci.*, **38**, 825–837.

Ziegler, C. L., and E. N. Rasmussen, 1998: The initiation of moist convection at the dryline: Forecasting issues from a case perspective. *Wea. Forecasting*, **13**, 1106–1131, doi:10.1175/1520-0434(1998)013<1106:TIOMCA>2.0.CO;2.